PURPOSE-LED PUBLISHING™

PAPER • **OPEN ACCESS**

Effect of capping on the Dirac semimetal Cd_3As_2 on Si grown via molecular beam epitaxy

To cite this article: Wei-Chen Lin *et al* 2025 *Nanotechnology* **36** 165001

OPEN ACCESS
IOP Publishing
Nanotechnology

Nanotechnology **36** (2025) 165001 (7pp)
https://doi.org/10.1088/1361-6528/adbb74

Effect of capping on the Dirac semimetal Cd_3As_2 on Si grown via molecular beam epitaxy

Wei-Chen Lin[1,2,3], Chiashain Chuang[4,5,*], Chun-Wei Kuo[4], Meng-Ting Wu[4], Jie-Ying Lee[6], Hsin-Hsuan Lee[7], Cheng-Hsueh Yang[6], Ji-Wei Ci[4], Tian-Shun Xie[8], Kenji Watanabe[9], Takashi Taniguchi[10], Nobuyuki Aoki[8], Jyh-Shyang Wang[5,7,*] and Chi-Te Liang[6,11,12,13,*]

[1] Department of Engineering and System Science, National Tsing Hua University, Hsinchu 300, Taiwan
[2] Taiwan International Graduate Program, Academia Sinica, Taipei 115, Taiwan
[3] Physical Measurement Laboratory, National Institute of Standards and Technology (NIST), Gaithersburg, MD 20899, United States of America
[4] Department of Electronic Engineering, Chung Yuan Christian University, Taoyuan 320, Taiwan
[5] Research Centre for Semiconductor Materials and Advanced Optics, Chung Yuan Christian University, Taoyuan 320, Taiwan
[6] Department of Physics, National Taiwan University, Taipei 106, Taiwan
[7] Department of Physics, Chung Yuan Christian University, Taoyuan 320, Taiwan
[8] Department of Materials Science, Chiba University, Chiba 263, Japan
[9] Research Center for Electronic and Optical Materials, National Institute for Materials Science, Tsukuba 305, Japan
[10] Research Center for Materials Nanoarchitectonics, National Institute for Materials Science, Tsukuba 305, Japan
[11] Centre for Quantum Science and Engineering, National Taiwan University, Taipei 106, Taiwan
[12] Taiwan Consortium of Emergent Crystalline Materials (TCECM), Taipei 106, Taiwan
[13] Taiwan Semiconductor Research Institute (TSRI), Hsinchu 300, Taiwan

E-mail: chiashain@cycu.edu.tw, jswang@cycu.edu.tw and ctliang@phys.ntu.edu.tw

Received 16 January 2025, revised 22 February 2025
Accepted for publication 28 February 2025
Published 10 March 2025

Abstract

Given the promising applications of large magnetoresistance in the Dirac semimetal cadmium arsenide (Cd_3As_2), extensive research into Si-compatible Cd_3As_2 devices is highly desirable. To prevent surface degradation and oxidation, the implementation of a protection layer on Cd_3As_2 is imperative. In this study, two vastly different protecting layers were prepared on top of two Cd_3As_2 samples. A zinc telluride layer was grown on top of one Cd_3As_2 film, giving rise to a ten-fold increased mobility, compared to that of the pristine Cd_3As_2 sample. Interestingly, unusual negative magnetoresistance is observed in the hexagonal boron nitride-capped Cd_3As_2 device when a magnetic field is applied perpendicularly to the Cd_3As_2 plane. This is in sharp

* Authors to whom any correspondence should be addressed.

contrast to the chiral anomaly that requires a magnetic field parallel to the Cd_3As_2 plane. We suggest that a protection layer on molecular beam epitaxy-grown Cd_3As_2 should be useful for realising its great device applications in magnetic sensing.

Supplementary material for this article is available online

Keywords: anomalous negative magnetoresistance, Dirac semimetal, Cd_3As_2 heterostructure

1. Introduction

Depending on the crystal orientation, cadmium arsenide (Cd_3As_2) can have a Dirac semimetallic phase [1, 2] or a topological insulating phase [3]. A Dirac semimetallic Cd_3As_2 exhibits a pronounced large linear magnetoresistance (LMR) phenomenon under a magnetic field perpendicular to the electric field direction, stemming from its linear band structure around the Dirac cone within the momentum space [4, 5] and the positive *g*-factor [6, 7]. Furthermore, with a parallel magnetic field, negative magnetoresistance (NMR) occurs due to the formation of the Fermi arc via the surface state [8]. Both aforementioned unique properties reveal Cd_3As_2 with promising applications in magnetic sensors, random access memory (RAM), *etc*. It is known that 3D Dirac semimetal Cd_3As_2 can support tunable epsilon-near-zero phenomena [9] and plasmonic waveguides [10] in the THz region. At present, there are some attempts to prepare high-quality Cd_3As_2 on Si (001) substrates [11]. This approach is highly desirable since such Cd_3As_2 layers are fully compatible with the existing silicon CMOS technology. Our approach is somewhat different as we use a Si (111) substrate for growing Cd_3As_2 films by molecular beam epitaxy (MBE). Importantly, our method may ultimately allow us to even combine GaN-based high-power and optoelectronic devices with the 3D Dirac semimetal and Si CMOS devices since AlN and AlGaN buffer layers can be readily grown on Si (111) so as to prepare high-quality GaN layers [12]. Moreover, Cd_3As_2 could be dramatically affected by water molecules in the ambient atmosphere [13]. Thus, a protection layer on Cd_3As_2 on Si (111) is highly imperative.

In this study, distinct from the seminal work done by Lygo *et al* which shows Cd_3As_2 as a topological insulator on the GaSb substrate [14], our Cd_3As_2 samples were grown on silicon (111) substrates. On the top, zinc telluride (ZnTe) was chosen as one of the protection layers covering the Cd_3As_2 sample owing to the suitable lattice constant compared to that of Cd_3As_2. Recently, Prof. Z-M Liao's group proposed a 2D–3D Dirac van der Waals graphene-Cd_3As_2 heterostructure device that should be promising for future spintronic electronics due to the interesting interlayer coupling, like charge transfer, band engineering, and lattice strain and so on [15, 16]. Consequently, for the second device, instead of graphene, we transferred 'white graphene'—hexagonal boron nitride (h-BN) flake as a 'modulation' on Cd_3As_2 Hall bar central channel on Si substrate as new 2D–3D van der Waals heterostructure device. With a light penetrative protection layer, the h-BN flake on Cd_3As_2 device becomes an ideal platform for testing the chiral light amplification [17] and probing the helicity-dependent photocurrent [18]. Furthermore, the capping protection idea may prove vital for topological nodal line semimetals [19].

Note that the linear band structure of the Dirac cone and Weyl nodes are topologically protected by the C4 crystalline symmetry because of the three-dimensional nature [20, 21]. Therefore, with the protection layers on top, both the ZnTe and h-BN protected Cd_3As_2 samples still retain the Weyl semimetallic properties evidenced by the notable NMR in a parallel magnetic field. Moreover, the ZnTe/Cd_3As_2 device manifests a significant enhancement in mobility by an order of magnitude, suggesting the efficacy of the ZnTe protective layer in preserving the integrity of Cd_3As_2. Conversely, although the mobility in the h-BN flake on Cd_3As_2 device only increases by a factor of three compared to that of the pristine Cd_3As_2 device, an unconventional NMR behaviour under a perpendicular magnetic field arises. We discuss a possible mechanism leading to this unexpected behaviour and show the improving characteristics of the protection layer-capped Cd_3As_2 with promising applications.

2. Results

Our experiments were performed on the Cd_3As_2 films grown on silicon substrates both with and without protection layers as shown in figure 1. The Cd_3As_2 layer was grown via the MBE technique, employing a silicon (111) substrate with an approximately 20 nm-thick-cadmium zinc telluride (CdZnTe) buffer layer. The thin CdZnTe buffer layer served to effectively mitigate the inherent lattice mismatch between Cd_3As_2 and the silicon substrate (see Methods). All these samples are compatible with existing Si CMOS technology, which is useful for potential device applications and integration with Si-based devices such as Si photonics [22–24], MOSFETs [24–27], and Si-based quantum information [28–30] and quantum processing [30–32]. The orientation of the Cd_3As_2 has been confirmed in the (112) direction via the x-ray diffraction (XRD) result (figure S1) which possesses the Dirac semi-metallic phase [33–39]. Moreover, the XRD data shows a piece of evidence that there exists a strain affecting the lattice at the interface because of a large lattice mismatch which reaches 68% between Cd_3As_2 and the h-BN capping layer (see supplementary section 1), where the lattice mismatch between Cd_3As_2 and ZnTe is 3.4% which can be negligible [35].

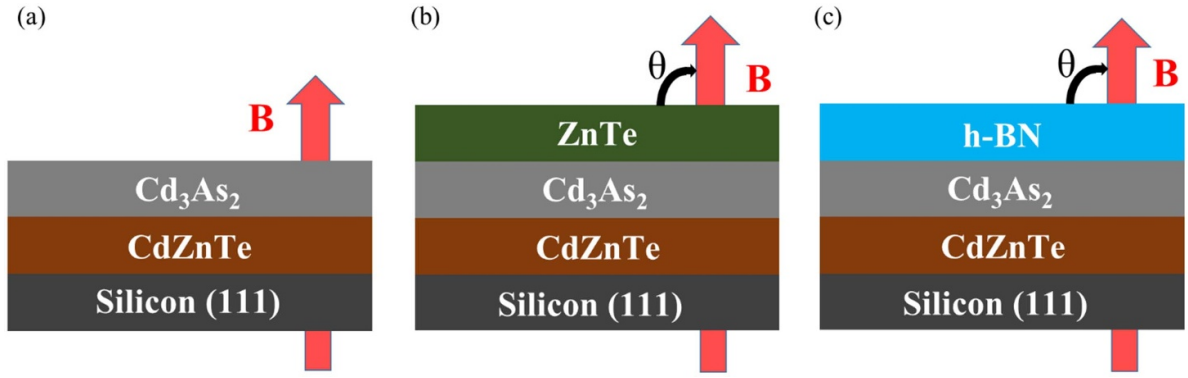

Figure 1. Schematics of the devices. (a) A pristine Cd_3As_2 sample, (b) a Cd_3As_2 sample with a ZnTe layer encapsulated, and (c) a Cd_3As_2 sample with a multilayer h-BN flake on top serving as a protective layer. Note that due to the limited size of the exfoliated h-BN, the area covered by h-BN is limited.

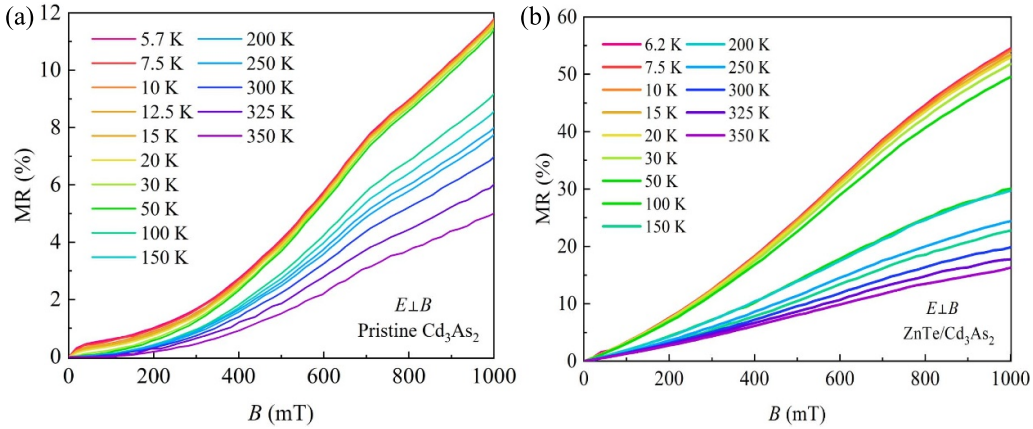

Figure 2. The characteristics of large MR. (a) The magnitude of the pristine Cd_3As_2 device reaches 12% at 5.7 K under 1000 mT. (b) The ZnTe/Cd_3As_2 device shows approximately 5 time of magnitude larger than the pristine Cd_3As_2 device indicating that ZnTe as a suitable protection layer for Cd_3As_2.

2.1. ZnTe-encapsulated Cd_3As_2

A 10 nm-thick-ZnTe protection layer was chosen due to its closely matched lattice constant compared to that of Cd_3As_2. The ZnTe protection layer was immediately grown at the same substrate temperature after completing the Cd_3As_2 layer for one minute, forming an initial layer which is about 1–2 nm thick. Growth is then paused, and the substrate temperature is raised to 230 °C before resuming ZnTe growth for seven minutes. This process results in a total ZnTe thickness of approximately 10 nm, including the initial low-temperature layer. This approach is necessary because the optimal substrate temperature for ZnTe epitaxy is 100 °C higher compared to that of Cd_3As_2. If ZnTe were grown with the same temperature which was used for Cd_3As_2, the crystalline quality would be significantly affected. However, directly increasing the substrate temperature while the Cd_3As_2 surface is exposed would cause degradation. As a result, a thin ZnTe layer is first grown at the same temperature as Cd_3As_2, providing a protective covering. The Ag contacts are deposited after the ZnTe protection layer is grown (see supplementary section 3).

As depicted in figure 2(b), the ZnTe/Cd_3As_2 device demonstrates significantly large LMR, reaching up to 55% at 1000 mT and 6.2 K, surpassing that in the pristine Cd_3As_2 device with a value of 12% at 1000 mT at 5.7 K (figure 2(a)). This highlights potential applications of the ZnTe/Cd_3As_2 device in RAM and magnetic sensors. Additionally, the ZnTe protection layer on Cd_3As_2 diminishes the effectiveness of vacuum annealing (see supplementary section 4), pointing out the exceptional insulating property of ZnTe.

Moreover, a significantly low carrier density and high mobility in the ZnTe/Cd_3As_2 device exhibit ZnTe itself as a promising protection layer which greatly improves the electrical properties of the Cd_3As_2 device (figure 3(b)). The mobility of the ZnTe/Cd_3As_2 device shows higher magnitude not only compared to the graphene/Cd_3As_2 heterostructure device ($\mu \approx 1.3 \times 10^4$ $cm^2V^{-1}s^{-1}$) [15] but also to the h-BN flake on Cd_3As_2 device (figure 3(c)). This underscores the advantage of selecting a capping layer with a lattice constant comparable to that of Cd_3As_2 for optimal device performance. The observed vastly different temperature dependence of mobility and carrier density between pristine Cd_3As_2

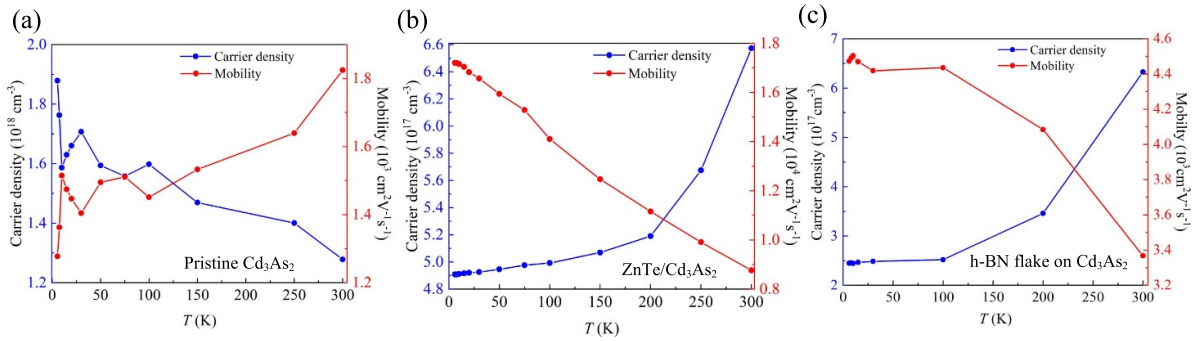

Figure 3. Carrier density and mobility modification via protection layers after vacuum anneal at 100 °C for 10 s. (a) The carrier density (mobility) of the pristine Cd_3As_2 device shows roughly unchanged compared to those of the other two devices. (b) and (c) In contrast, the ZnTe/Cd_3As_2 device and the h-BN flake on Cd_3As_2 device show a different trend compared to the pristine Cd_3As device where the carrier density (mobility) decreases (increases) while the temperature decreases. However, the ZnTe protection layer renders the vacuum annealing less effective. The pristine Cd_3As_2 device manifests the highest carrier density and the lowest mobility amongst the three Cd_3As_2 devices at the lowest temperature. These characterizations point out that the insulating protection layers significantly enhance the electrical properties of the underlying Cd_3As_2.

layer and its ZnTe and h-BN capped counterparts can be explained in the following. In capped films, the carrier density appears to increase with increasing temperature. This may be ascribed to charge trapping effect, which can be observed in graphene on SiC [40]. The capped Cd_3As_2 devices show metallic behaviour in the sense that the mobility decreases with increasing temperature (electron-phonon scattering). In contrast, the pristine Cd_3As_2 layer shows weakly insulating behaviour where $dR/dT < 0$ since the amount of disorder is strong due to molecular absorbates on the Cd_3As_2 surface. Consequently, the mobility increases slightly with increasing temperature.

The NMR depicted in figure 4(a) highlights the emergence of the chiral anomaly as time reversal symmetry breaks due to an external magnetic field parallel to the direction of current flow in the ZnTe/Cd_3As_2 device. Furthermore, the angle-dependent MR measurements (figure 4(b)) provide compelling evidence of the occurrence of the chiral anomaly [21, 41, 42]. For $T > 75$ K, the crossover from positive to negative MR diminishes as the chiral anomaly is expected to become weaker with increasing temperature [21]. This temperature is significantly lower than the transition temperature $T_c \approx 234.5$ K for which there is a crossover from metallic ($dR/dT > 0$) to weakly insulating behaviour ($dR/dT < 0$) (supplementary figure 4(b)). Our results thus suggest that the zero-field metallic behaviour ($dR/dT > 0$) does not guarantee the chiral anomaly.

2.2. H-BN flake on Cd_3As_2

High-quality h-BN flakes were mechanically exfoliated and stacked onto the Cd_3As_2 surface by a standard dry transfer technique (see Methods). The inset of figure 5(a) illustrates slightly asymmetric MR under perpendicular magnetic fields in opposite directions. The unintended mixing of the longitudinal resistivity with the Hall resistivity may lead to the observed asymmetric MR [43]. For simplicity, only the positive magnetic field data will be presented in the subsequent part of our manuscript.

Rock-solid evidence of the chiral anomaly, shown as the red curve in figure 5(b), is exhibited in the h-BN flake on Cd_3As_2 device. Figure 5(a) shows anomalous NMR in a perpendicular magnetic field at various temperatures, a phenomenon distinct from the chiral anomaly that requires the assistance of a magnetic field parallel to the current flow direction. The anomalous NMR is attributed to the transition from weak anti-localization to weak localization effect (see supplementary section 6) rendering from the spatial inversion symmetry breaking due to the strain-gradient on Cd_3As_2 central channel so as to induce a topological transition [16, 44]. This picture is consistent with shifted Cd_3As_2 peaks observed in the XRD data (figure S1). The observed magnetoresistance in our h-BN capped Cd_3As_2 is interesting. Although we cannot pinpoint the exact underlying mechanism, we speculate that the interface interaction/effect should play an important role in this. Such an interface effect plays a role in the spin-related Khosla–Fischer type MR, *i.e.* an interesting, similar PMR/NMR/PMR crossover is observed in ferromagnetic α-Fe_2O_3 nanosheet grown on MoS_2 [45].

From the angle-dependent MR (figure 5(b)), the negative response tends to be more pronounced as the magnetic field direction aligns perpendicularly to the current direction, providing convincing evidence of the anomalous NMR in the h-BN flake on the h-BN flake on Cd_3As_2 device. The aforementioned observations underscore the advantages of utilizing the h-BN flake as a protection layer and show promising applications of the h-BN flake on Cd_3As_2 device. Please note that the carrier densities are different between figures 5(a) and (b) because the measurements were performed in different thermal cycles.

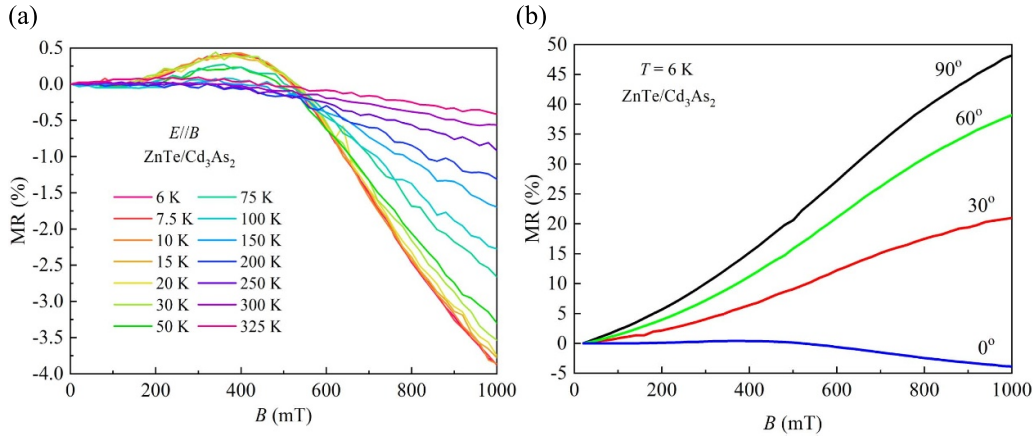

Figure 4. The chiral anomaly evidenced by the NMR observed in the $ZnTe/Cd_3As_2$ device. (a) The persistence of NMR under a parallel magnetic field at elevated temperatures, particularly at room temperature, suggests the robust presence of the chiral anomaly in the $ZnTe/Cd_3As_2$ device. (b) MR plotted with different tilted angles at 6 K. The magnitude of MR decreases while the magnetic field angle tilts from perpendicular (90°) to parallel (0°) direction.

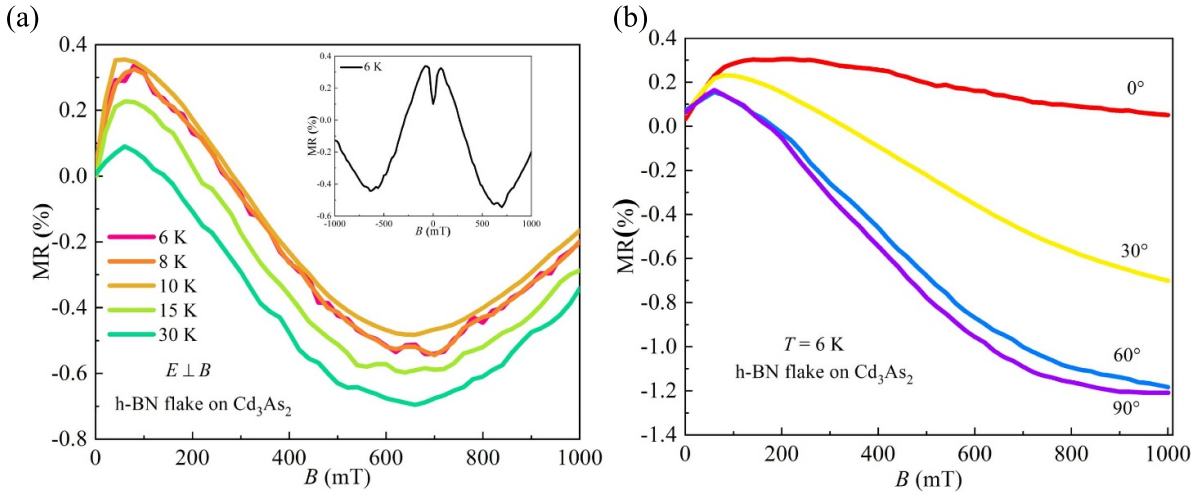

Figure 5. MR in the h-BN flake on Cd_3As_2 device. (a) NMR under a perpendicular magnetic field. As the temperature increases, the negative behaviour diminishes. The inset shows the symmetrical MR from −1000 mT to 1000 mT. (b) Angle-dependent on the MR at 6 K. The magnitude of the negative response intensifies as the magnetic field direction shifts from parallel (0°) to perpendicular (90°) orientation.

3. Discussion

In contrast to the pristine Cd_3As_2 device, the $ZnTe/Cd_3As_2$ and the h-BN flake on Cd_3As_2 device both demonstrate mobility enhancements. Notably, the $ZnTe/Cd_3As_2$ device shows an order of magnitude increase. Such a ten-fold mobility enhancement is mostly ascribed to the almost lattice-matched ZnTe layer (with Cd_3As_2), which improves the interface/crystal quality. Moreover, the ZnTe protection layer places any molecular adsorbates far away from the actual active Cd_3As_2 layer, thereby decreasing electron-impurity scattering. In the case of h-BN capped Cd_3As_2, the large lattice mismatch between h-BN and Cd_3As_2 introduces strain. Therefore, the mobility enhancement is lower compared with that of its ZnTe capped counterpart. Furthermore, the $ZnTe/Cd_3As_2$ device exhibits a significant increase in the LMR which surpasses the magnitude shown in the pristine Cd_3As_2. These improvements strongly suggest the advantage of selecting a capping layer with a closely matched lattice constant. Interestingly, the h-BN flake on Cd_3As_2 device presents an anomalous NMR behaviour in a perpendicular magnetic field which is attributed to the strain-gradient-induced breaking of spatial inversion symmetry due to significant lattice mismatch, triggering a topological transition in Cd_3As_2. In summary, our findings underscore the potential of capping Cd_3As_2 on silicon substrates to enhance device performance and enable novel magnetoresistance effects. Therefore, optimizing with various capping layers could prove pivotal for subsequent studies in the future.

4. Methods

4.1. Cd_3As_2 film growth

Following the fabrication procedures in [35], our Cd_3As_2 samples were grown on a Si (111) substrate by MBE. The qualities of our Cd_3As_2 samples were optimized by the XRD

image shown in the supplementary section 1. We replaced the additional buffer layer of ZnTe with CdZnTe to minimize the lattice mismatch from 3.4% to around 1% at the interface between the buffer layer and Cd_3As_2. The ZnTe protection layer was grown after the annealing process.

4.2. Cd_3As_2 Hall bar

The Hall bar configurations of the pristine Cd_3As_2 and an h-BN flake on Cd_3As_2 samples were shaped by reactive ion etching with 10 sccm CF_4 and 10 sccm Ar introduced for 5 min. The average thickness of Cd_3As_2 film on the Hall bar region is 175 nm (see figure S3).

4.3. H-BN dry transfer technique

We employed a standard dry transfer technique based on the concept described in Wang *et al* [46]. Firstly, polycarbonate (PC) was placed on a homemade polydimethylsiloxane substrate. Subsequently, the PC was used to pick up the h-BN flake from the SiO_2/Si substrate. Afterwards, the h-BN flake was released onto the central region of the Cd_3As_2 with a Hall bar configuration by heating up the transfer stage. During this process, the PC was melted and left on the h-BN flake on Cd_3As_2 device. Finally, chloroform was utilized to clean the PC residual.

4.4. Characterizations

The four-terminal measurements were performed to eliminate the contact resistance in a closed cycle cryostat and equipped with a 1 T magnet with rotational field angles.

Data availability statement

The data that support the findings of this study are available upon reasonable request from the authors.

Acknowledgment

This work was funded by the Ministry of Science and Technology (MOST) and the National Science and Technology Council (NSTC), Taiwan (Grant Nos: NSTC 110-2112-M-033-009-MY3, NSTC 112-2221-E-033-040, NSTC 113-2112-M-033-013, NSTC 113-2221-E-033-023, and NSTC 113-2112-M-002-034-MY3). CC acknowledges the Higher Education Sprout Project in Chung Yuan Christian University which allowed him to visit sister university - Chiba University, Japan for supporting this topic. KW and TT acknowledge support from JSPS KAKENHI (Grant Numbers 19H05790, 20H00354 and 21H05233).

ORCID iDs

Wei-Chen Lin https://orcid.org/0009-0003-9542-3697
Chiashain Chuang https://orcid.org/0000-0002-7677-8121
Kenji Watanabe https://orcid.org/0000-0003-3701-8119
Nobuyuki Aoki https://orcid.org/0000-0001-9203-6040
Chi-Te Liang https://orcid.org/0000-0003-4435-5949

References

[1] Li C-Z, Li J-G, Wang L-X, Zhang L, Zhang J-M, Yu D and Liao Z-M 2016 Two-carrier transport induced Hall anomaly and large tunable magnetoresistance in Dirac semimetal Cd_3As_2 nanoplates *ACS Nano* **10** 6020–8
[2] Ouyang W, Lygo A C, Chen Y, Zheng H, Vu D, Wooten B L, Liang X, Heremans J P, Stemmer S and Liao B 2024 Extraordinary thermoelectric properties of topological surface states in quantum-confined Cd_3As_2 thin films *Adv. Mater.* **36** 2311644
[3] Munyan S, Rashidi A, Lygo A C, Kealhofer R and Stemmer S 2023 Edge channel transmission through a quantum point contact in the two-dimensional topological insulator cadmium arsenide *Nano Lett.* **23** 5648
[4] Wang C and Lei X 2012 Linear magnetoresistance on the topological surface *Phys. Rev.* B **86** 035442
[5] Abrikosov A 1998 Quantum magnetoresistance *Phys. Rev.* B **58** 2788
[6] Singh M and Wallace P 1983 Effect of 'free-electron' terms on the g-factor of Cd_3As_2 *Solid State Commun.* **45** 9
[7] Wallace P 1979 Electronic g-factor in Cd_3As_2 *Phys. Status Solidi* b **92** 49
[8] Wang Z, Weng H, Wu Q, Dai X and Fang Z 2013 Three-dimensional Dirac semimetal and quantum transport in Cd_3As_2 *Phys. Rev.* B **88** 125427
[9] Cheng Y, Cao W and He X 2024 Hybrid plasmonic waveguides with tunable ENZ phenomenon supported by 3D Dirac semimetals *Laser Photonics Rev.* **18** 2400167
[10] Wang G, Cao W and He X 2023 3D Dirac semimetal elliptical fiber supported THz tunable hybrid plasmonic waveguides *IEEE J. Sel. Top. Quantum Electron.* **29** 8400207
[11] Rice A and Alberi K 2023 Epitaxial integration of Dirac semimetals with Si (001) *Crystal* **13** 578
[12] Lee J-H and Im K-S 2021 Growth of high quality GaN on Si (111) substrate by using two-step growth method for vertical power devices application *Crystal* **11** 234
[13] Zhang Y, Nappini S, Sankar R, Bondino F, Gao J and Politano A 2021 Assessing the stability of Cd_3As_2 Dirac semimetal in humid environments: the influence of defects, steps and surface oxidation *J. Mater. Chem.* C **9** 1235
[14] Lygo A C, Guo B, Rashidi A, Huang V, Cuadros-Romero P and Stemmer S 2023 Two-dimensional topological insulator state in cadmium arsenide thin films *Phys. Rev. Lett.* **130** 046201
[15] Wu Y-F, Zhang L, Li C-Z, Zhang Z-S, Liu S, Liao Z-M and Yu D 2018 Dirac semimetal heterostructures: 3D Cd_3As_2 on 2D graphene *Adv. Mater.* **30** 1707547
[16] Zheng W Z, Zhao T-Y, Wang A-Q, Xu D-Y, Xiang P-Z, Ye X-G and Liao Z-M 2021 Strain-gradient induced topological transition in bent nanoribbons of the Dirac semimetal Cd_3As_2 *Phys. Rev.* B **104** 155140
[17] Nishida Y 2023 Chiral light amplifier with pumped Weyl semimetals *Phys. Rev. Lett.* **130** 096903
[18] Wang B M, Zhu Y, Travaglini H C, Sun R, Savrasov S Y, Hahn W, van Benthem K and Yu D 2023 Spatially dispersive helicity-dependent photocurrent in Dirac semimetal Cd_3As_2 nanobelts *Phys. Rev.* B **108** 165405
[19] Tian Q, Bagheri Tagani M, Izadi Vishkayi S, Zhang C, Li B, Zhang L, Yin L-J, Tian Y, Zhang L and Qin Z 2024 Twist-angle tuning of electronic structure in

two-dimensional Dirac nodal line semimetal Au_2Ge on Au (111) *ACS Nano* **18** 9011
[20] Liang S *et al* 2018 Experimental tests of the chiral anomaly magnetoresistance in the Dirac-Weyl semimetals Na_3Bi and GdPtBi *Phys. Rev.* X **8** 031002
[21] Ong N and Liang S 2021 Experimental signatures of the chiral anomaly in Dirac–Weyl semimetals *Nat. Rev. Phys.* **3** 394
[22] Luo Y, Chamanzar M, Apuzzo A, Salas-Montiel R, Nguyen K N, Blaize S and Adibi A 2015 On-chip hybrid photonic–plasmonic light concentrator for nanofocusing in an integrated silicon photonics platform *Nano Lett.* **15** 849
[23] Majumdar A, Kim J, Vuckovic J and Wang F 2013 Electrical control of silicon photonic crystal cavity by graphene *Nano Lett.* **13** 515
[24] Shu H *et al* 2022 Microcomb-driven silicon photonic systems *Nature* **605** 457
[25] Fujiwara A and Takahashi Y 2001 Manipulation of elementary charge in a silicon charge-coupled device *Nature* **410** 560
[26] Convertino C, Zota C B, Schmid H, Caimi D, Czornomaz L, Ionescu A M and Moselund K E 2021 A hybrid III–V tunnel FET and MOSFET technology platform integrated on silicon *Nat. Electron.* **4** 162
[27] Liu H, Neal A T and Ye P D 2012 Channel length scaling of MoS_2 MOSFETs *ACS Nano* **6** 8563
[28] Veldhorst M *et al* 2015 A two-qubit logic gate in silicon *Nature* **526** 410
[29] Maurand R *et al* 2016 A CMOS silicon spin qubit *Nat. Commun.* **7** 13575
[30] Tosi G, Mohiyaddin F A, Schmitt V, Tenberg S, Rahman R, Klimeck G and Morello A 2017 Silicon quantum processor with robust long-distance qubit couplings *Nat. Commun.* **8** 450
[31] Watson T *et al* 2018 A programmable two-qubit quantum processor in silicon *Nature* **555** 633
[32] Qiang X *et al* 2018 Large-scale silicon quantum photonics implementing arbitrary two-qubit processing *Nat. Photon.* **12** 534
[33] Schumann T, Goyal M, Kim H and Stemmer S 2016 Molecular beam epitaxy of Cd_3As_2 on a III–V substrate *APL Mater.* **4** 126110
[34] Rice A D, Lee C H, Fluegel B, Norman A G, Nelson J N, Jiang C S, Steger M, McGott D L, Walker P and Alberi K 2022 Epitaxial Dirac semimetal vertical heterostructures for advanced device architectures *Adv. Funct. Mater.* **32** 2111470
[35] Lin W-C *et al* 2024 Chiral anomaly and Weyl orbit in three-dimensional Dirac semimetal Cd_3As_2 grown on Si *Nanotechnology* **35** 165002
[36] Borisenko S, Gibson Q, Evtushinsky D, Zabolotnyy V, Büchner B and Cava R J 2014 Experimental realization of a three-dimensional Dirac semimetal *Phys. Rev. Lett.* **113** 027603
[37] Xiao R, Islam S, Yanez W, Ou Y, Liu H, Xie X, Chamorro J, McQueen T M and Samarth N 2023 Influence of magnetic and electric fields on universal conductance fluctuations in thin films of the dirac semimetal Cd_3As_2 *Nano Lett.* **23** 5634
[38] Wang H *et al* 2019 Magnetic field-enhanced thermoelectric performance in Dirac semimetal Cd_3As_2 crystals with different carrier concentrations *Adv. Funct. Mater.* **29** 1902437
[39] Gao J, Cupolillo A, Nappini S, Bondino F, Edla R, Fabio V, Sankar R, Zhang Y-W, Chiarello G and Politano A 2019 Surface reconstruction, oxidation mechanism, and stability of Cd_3As_2 *Adv. Funct. Mater.* **29** 1900965
[40] Farmer D B, Perebeinos V, Lin Y-M, Dimitrakopoulos C and Avouris P 2011 Charge trapping and scattering in epitaxial graphene *Phys. Rev.* B **84** 205417
[41] Wang L-X, Li C-Z, Yu D-P and Liao Z-M 2016 Aharonov–Bohm oscillations in Dirac semimetal Cd_3As_2 nanowires *Nat. Commun.* **7** 10769
[42] Li Q, Kharzeev D E, Zhang C, Huang Y, Pletikosić I, Fedorov A, Zhong R, Schneeloch J, Gu G and Valla T 2016 Chiral magnetic effect in $ZrTe_5$ *Nat. Phys.* **12** 550
[43] Li C, de Ronde B, Nikitin A, Huang Y, Golden M S, de Visser A and Brinkman A 2017 Interaction between counterpropagating quantum Hall edge channels in the 3D topological insulator $BiSbTeSe_2$ *Phys. Rev.* B **96** 195427
[44] Ivanov V, Borkowski L, Wan X and Savrasov S Y 2024 Absence of backscattering in Fermi-arc mediated conductivity of the topological Dirac semimetal Cd_3As_2 *Phys. Rev.* B **109** 195139
[45] Debnath A, Bhattacharya S, Mondal T K, Tada H and Saha S K 2020 Giant enhancement in coercivity of ferromagnetic α-Fe_2O_3 nanosheet grown on MoS_2 *J. Appl. Phys.* **127** 013901
[46] Wang L *et al* 2013 One-dimensional electrical contact to a two-dimensional material *Science* **342** 614